MNRAS **000**, 1–14 (2015) Preprint 1 February 2017 Compiled using MNRAS LATEX style file v3.0

Unveiling slim accretion disc in AGN through X-ray and Infrared observations

Núria Castelló-Mor,[1⋆] Shai Kaspi,[1,2] Hagai Netzer,[1] Pu Du,[3] Chen Hu,[3] Luis C. Ho,[4,5] Jin-Ming Bai,[6] Wei-Hao Bian,[7] Ye-Fei Yuan,[8] Jian-Min Wang[3,9]

[1] *School of Physics and Astronomy, Tel Aviv University, Tel Aviv 69978, Israel*
[2] *Wise Observatory, School of Physics and Astronomy, Tel Aviv University, Tel Aviv 69978, Israel*
[3] *Key Laboratory for Particle Astrophysics, Institute of High Energy Physics, Chinese Academy of Sciences, 19B Yuquan Road, Beijing 100049, China*
[4] *Kavli Institute for Astronomy and Astrophysics, Peking University, Beijing 100871, China*
[5] *Department of Astronomy, School of Physics, Peking University, Beijing 100871, China*
[6] *Yunnan Observatories, Chinese Academy of Sciences, Kunming 650011, China*
[7] *Physics Department, Nanjing Normal University, Nanjing 210097, China*
[8] *Department of Astronomy, University of Science and Technology of China, Hefei 230026, China*
[9] *National Astronomical Observatories of China, Chinese Academy of Sciences, 20A Datun Road, Beijing 100020, China*

arXiv:1701.08781v1 [astro-ph.GA] 30 Jan 2017

Accepted XXX. Received YYY; in original form ZZZ

ABSTRACT

In this work, which is a continuation of Castelló-Mor et al. (2016), we present new X-ray and infrared (IR) data for a sample of active galactic nuclei (AGN) covering a wide range in Eddington ratio over a small luminosity range. In particular, we rigorously explore the dependence of the optical-to-X-ray spectral index α_{OX} and the IR-to-optical spectral index on the dimensionless accretion rate, $\dot{\mathcal{M}}= \dot{m}/\eta$ where $\dot{m}= L_{AGN}/L_{Edd}$ and η is the mass-to-radiation conversion efficiency, in low and high accretion rate sources. We find that the SED of the faster accreting sources are surprisingly similar to those from the comparison sample of sources with lower accretion rate. In particular: I) the optical-to-UV AGN SED of slow and fast accreting AGN can be fitted with thin AD models. II) The value of α_{OX} is very similar in slow and fast accreting systems up to a dimensionless accretion rate $\dot{\mathcal{M}}_c \sim$10. We only find a correlation between α_{OX} and $\dot{\mathcal{M}}$ for sources with $\dot{\mathcal{M}}>\dot{\mathcal{M}}_c$. In such cases, the faster accreting sources appear to have systematically larger α_{OX} values. III) We also find that the torus in the faster accreting systems seems to be less efficient in reprocessing the primary AGN radiation having lower IR-to-optical spectral slopes.

These findings, failing to recover the predicted differences between the SEDs of slim and thin ADs within the observed spectral window, suggest that additional physical processes or very special geometry act to reduce the extreme UV radiation in fast accreting AGN. This may be related to photon trapping, strong winds, and perhaps other yet unknown physical processes.

Key words: galaxy – quasar – Seyfert

1 INTRODUCTION

This work is a continuation of our previous paper (Castelló-Mor et al. 2016) where we studied the properties of thin and slim accretion discs (AD) in active galactic nuclei (AGN). Theory postulated profound differences between the typical spectral energy distribution (SED) of slow and fast accreting black holes (BHs) (Wang & Zhou 1999; Mineshige et al. 2000). In slow accreting systems, the primary emission of the AGN is well determined by the standard thin AD theory (Shakura & Sunyaev 1973, hereafter SS73), where the total luminosity emitted by the AGN, L_{AGN}, is set by the accretion rate ($\dot{m}= L_{AGN}/L_{Edd}$) and the mass-to-radiation conversion efficiency, η, which, in itself, depends on the BH spin. The direct integration of the disc SED is not practical in almost all cases, because much of the radiation is emitted beyond the Lyman limit at 912 Å. To avoid the dependence on the BH spin, which sets the total emitted radiation in thin

⋆ E-mail: nuria@wise.tau.ac.il (TAU)

© 2015 The Authors

ADs, a dimensionless accretion rate $\dot{\mathcal{M}}$ can be introduced

$$\dot{\mathcal{M}} \equiv \dot{m}/\eta \simeq 20.1 \left(\frac{l_{44}}{\cos i}\right)^{3/2} M_7^{-2} \quad (1)$$

where $M_7 = M_{BH}/10^7 M_\odot$, i the inclination angle and l_{44} the luminosity at 5100Å in units of 10^{44} erg/s (see Frank et al. 2002; Netzer 2013; Du et al. 2015). Thus, for $\dot{m}$=1, a non-rotating BH results in $\dot{\mathcal{M}}$= 17.54 and a maximally prograde rotating BH gives $\dot{\mathcal{M}}$=3.1.

The BH governs a wide range of observed AGN properties such as spectral slopes and other emission properties. It also affects the geometry of the AD. Beyond a critical mass accretion rate $\dot{\mathcal{M}}_c$, energy transport by advection dominates over radiative in the inner parts of the system and the disc is thought to become geometrically thick, or slim ("slim accretion disc", Abramowicz et al. 1988; Laor & Netzer 1989; Wang & Zhou 1999; Sądowski et al. 2011; Kawakatu & Ohsuga 2011). In such cases, the standard AD model breaks down and processes that are not important in geometrically thin ADs must be taken into account. Theoretical works (Wang & Zhou 1999; Mineshige et al. 2000) suggest that in the slim disc regime, photon trapping, followed by radial advection, reduces the mass-to-radiation efficiency leading to saturated luminosity. In particular, the physics related to the innermost stable orbit changes dramatically and the BH spin is not affecting the radiation efficiency factor η. While these general ideas have been suggested in numerous slim disc calculations, they are not confirmed by recent numerical simulations (Sądowski & Narayan 2016, and references therein) which indicate that radial advection is far less important than estimated by the earlier models. They also suggest that much of the released energy can be via disc winds and the fraction of emitted radiation, its SED and angular pattern, are highly uncertain. There are also disagreements among the various simulations (see e.g. Jiang et al. 2014) indicating how immature this field is. Other works, such us (Collin & Kawaguchi 2004), are focused on the intrinsic characteristics of the general population.

Slim AD systems are thought to have extreme X-ray properties. The reason is not fully understood with the best explanations so far relating this to the conditions in the X-ray emitting corona via Comptonization, photon trapping, magnetorotational instabilities, and extreme radiation pressure force (see review in Wang et al. 2013).

When comparing thin to slim accretion discs it is important to note that in both systems, the observed 5100Å emission (l_{44}) is thought to originate at large enough radii and thus is less influenced by the radial motion of the accretion flow compared with the regions closer in that emit the shorter wavelength photons. At these large radii Eq. 1 is a reliable way to determine the normalized mass accretion rate of slim AD systems.

Following earlier works on slim ADs (e.g. Du et al. 2015, and references therein), we classified candidates to host slim discs as those objects with $\dot{m}$= $\eta\dot{\mathcal{M}}\geq$0.1. This is based on both the thickening of the disc, as well as, general considerations about the onset of radial advection in the inner parts of the disc. Since we cannot observe the entire SED, we have no direct way to measure $\dot{m}$. To be conservative, we chose the lowest possible efficiency, η = 0.038 (retrograde accretion) to set a lower limit on the normalized accretion rate, $\dot{\mathcal{M}}$=2.63. For simplicity we change this rate slightly and assume that $\dot{\mathcal{M}}_{min}$ =3 is the requiered minimum normalzied accretion rate for a slim AD candidate.

In 2013 we started a large observational project aimed at understanding the faster accreting AGN in the local Universe. The first part of our project involved accurate determination of BH masses through reverberation mapping (RM, Du et al. 2014, 2015; Wang et al. 2014; Du et al. 2015), and hence its mass accretion rate. We found that fast accreting systems do not follow the well-known correlation between the typical broad line region (BLR) size, R_{BLR}, and the monochromatic luminosity at 5000 Å, $L_{5100\text{Å}}$, having lower BH masses for a given luminosity. We interpret this behaviour as a change in the geometry of the AD from thin to slim. Furthermore, Castelló-Mor et al. (2016) (hereafter paper I) compared IR-optical-UV-X-ray SEDs of 16 fast accreting systems ($\dot{\mathcal{M}}\geq\dot{\mathcal{M}}_{min}$) with RM-based BH masses, to a sample of 13 RM-mapped AGN with low accretion rates ($\dot{\mathcal{M}}<\dot{\mathcal{M}}_{min}$). While AD theory predicts slim AD systems to have much higher UV luminosity, observations falsify this prediction. In paper I, we see no evidence for extremely luminous ionizing continua, and no unusual torus emission (albeit from large aperture WISE data), in those sources expected to be powered by slim ADs. While the spectral differences between fast and slow accretors are indirect, since the observations do not reach far enough into the UV where slim and thin AD emit most of their radiation, it is hard to believe that the increase in the total disc luminosity expected in those AGN that are powered by slim ADs, is exactly compensated for by a changing geometry of the tours.

In this paper we expand the work to include larger AGN samples and new X-ray and IR data. The goal is to understand better the role of accretion rate in determining the physics of high Eddington ratio sources over a well defined, limited luminosity range and to critically test various suggestions about the differences between thin and slim ADs. In particular we want to compare the role of accretion rate on the 2 keV and 5μm emission in low and high Eddington ratio sources. Note that the limited luminosity range refers to the range in $L_{5100\text{Å}}$, not in the total luminosity emitted by the AGN, $L_{\rm AGN}$. The conversion to total luminosity involves the BH mass and spin and hence the limit on $L_{\rm AGN}$ is not constrained so well. Throughout the paper we make a clear distinction between fast accreting AGN and narrow-line Seyfert 1 (NLS1s) since many objects in the latter group are not necessarily high Eddington ratio sources.

The structure of the paper is as follows: In Section 2, we describe the sample used in this study, how we define low and high accretion rate AGN, and how BH mass and dimensionless accretion rate are estimated. In Section 3, we describe how the spectral properties of the AGN samples were deduced. The correlation analysis between α_{OX} and the new IR-to-optical spectral slope on the dimensionless accretion rate is presented in Section 4. Finally, in Section 5 we summarize our findings. In Appendix A, we present the X-ray spectral analysis for new RM-selected X-ray sources with the highest Eddington ratio up to now.

2 THE SAMPLE

The AGN employed in the present analysis are obtained from two different samples with the objective of spanning a

large range of accretion rates. From the 29 AGN presented in paper I, we select all the sources that have X-ray measurements. We then selected 15 out of the 29 AGN that have been observed by XMM-Newton in the past and four additional sources (J075101, J080101, J081441, and J100055) that have been recently observed by XMM-Newton especially for this project (PI: Shai Kaspi). These 19/29 objects (of which 11 have $\dot{\mathcal{M}}$<3) belong to a unique sample via RM (Du et al. 2014, 2015) and hence their BH mass was measured. As of early 2015, the sample include basically all the potential slim disc candidates which are bright enough in the optical/UV to have direct mass measurements (Du et al. 2015).

A complementary sample of 36 AGN were selected from the bright soft X-ray selected AGN sample of Grupe et al. (2010). Because the aim of our work is to investigate the connection of α_{OX} with the dimensionless accretion rate, this sample was selected to overlap in optical luminosity (defined as λL_λ at the rest-frame wavelength 5100Å) the luminosity of the RM-selected AGN sample. We note that this sample represents the largest number of AGN observed to study contemporaneous optical-to-X-ray observations within a well-defined luminosity range. Grupe et al. (2010) make the common assumption that the black hole mass scaling relation derived from RM-selected AGN sample is applicable to all AGN. However, Du et al. (2015) found that fast accreting AGN do not follow the well-known correlation between R_{BLR} and $L_{5100\text{Å}}$. This result was confirmed by the more recent study of Du et al. (2016a) where several additional objects with very high Eddington ratio are are included. In this work, the BH mass of the Grupe et al. (2010) AGN (hereafter *soft-X-ray-selected* AGN group) were estimated assuming that the R_{BLR}–$L_{5100\text{Å}}$ relationship is in fact a function of the mass accretion rate (see Section 2.1).

2.1 BH mass and dimensionless accretion rate

Direct determination of BH mass through RM (which is the most accurate technique) still only exist for a small fraction of all AGN (∼60), and bolometric luminosities are subject to large uncertainties about the extreme-UV part of the SED which is not directly observable. In the present paper we follow the Du et al. (2015) method to determine a dimensionless accretion rate, $\dot{\mathcal{M}}$, which is independent of the mass-to-radiation, spin-dependent conversion efficiency η (see Eq. 1). The equation we use is based on the standard way to calculate the accretion rate in the SS73 thin AD model (for more explanations see Frank et al. 2002; Netzer 2013). We assumed an inclination angle of $\cos i = 0.75$ which corresponds an inclination typical of type-I AGN that cannot be observed from a much larger inclination angle due to obscuration by the central torus.

For the RM-selected AGN group, the BH mass are taken from the RM papers and are based on measurements of the $FWHM(H\beta)$ method (see Du et al. 2015). For the soft-X-ray-selected AGN group, for which the BH mass is unknown, we need to distinguish between low and high mass accretion rate sources since the two groups are known to have different $R_{BLR} - L_{5100\text{Å}}$ relationships. We therefore use the following two-step approach. We compute M_{BH} based on the relationship found for slow accreting AGN (Kaspi et al. 2000; Bentz et al. 2009, 2013; Du et al. 2015). In this case $R_{BLR} = \mathcal{K} l_{44}^{\alpha}$ and the BH mass is

$$M_{BH} = 1.4625 \times 10^5 f_{BLR} \left(\frac{FWHM}{10^3 \mathrm{km/s}} \right)^2 \mathcal{K} l_{44}^{\alpha} \quad (2)$$

where FWHM is the full-width at half-maximum intensity of Hβ and f_{BLR} is a factor that includes information about the geometry and kinematics of the BLR gas. We assumed $f_{BLR} = 1$ in agreement with Du et al. (2015) and the recent work of Woo et al. (2015). The slope α and the scaling factor $\mathcal{K}$ differ slightly from one study to the next. In the first stage we estimate the BH mass and $\dot{\mathcal{M}}$ of the soft-X-ray-selected AGN using the $R_{BLR} - l_{44}$ correlation given by Bentz et al. (2013, $\mathcal{K} = 33.65$ and $\alpha = 0.53$) which assumes no dependence of R_{BLR} on the accretion rate. We then use equation 1 to obtain a rough estimate of $\dot{\mathcal{M}}$ and thus determine whether a dependece on accretion rate is necessary. As explained, the fiducial accretion rate we use to set the boundary between the two groups is $\dot{\mathcal{M}}_{min}$ =3, which corresponds to the minimum possible accretion rate to be selected as an slim AD system (see Introduction). According to Du et al. (2016a) for such objects

$$R_{BLR} = \mathcal{K} l_{44}^{\alpha} \ \min \left[1, \left(\frac{\dot{\mathcal{M}}}{\dot{\mathcal{M}}_c} \right)^{-\gamma} \right] \quad (3)$$

Unfortunately, this expression does not allow simple iteration on the BH mass since starting with the mass obtained in this way (i.e. the parameters used for the slow accreting systems) and calculating new M_{BH} and $\dot{\mathcal{M}}$ leads to divergence. We therefore followed a different procedure based on a different equation of the type $R_{BLR} = \mathcal{K} l_{44}^{\alpha}$, which is not meant to fit all high accretion rate sources, but rather to find a good approximation, over a limited luminosity range, that is changing continuously with $L_{5100\text{Å}}$ and is consistent with Eq. 3 for the sources with $\dot{\mathcal{M}} \geq \dot{\mathcal{M}}_{min}$. The parameters that fit these requirements very well are $\mathcal{K} = 14.96$ and $\alpha = 0.14$.

Fig. 1 illustrates the use of this method by comparing the best-fit R_{BLR}–l_{44} relationship obtained by fitting all the fast accreting sources with RM-measurements presented in paper I with the best fit relationship found for slow accreting systems (Bentz et al. 2013). The red points represent the BLR size given by the RM measurements. It is obvious that the best-fit relationship for slow accreting systems can not be used for sources with higher accretion rates. In Fig. 2, the estimated BH mass and accretion rate obtained by our approach (gray, step-filled histogram) are compared with the most recent R_{BLR}–$L_{5100\text{Å}}$ relationship (Bentz et al. 2013), which assumes no dependency on the mass accretion rate (blue, dashed-line histogram), and with the values used by Grupe et al. (2010, red, solid-line histogram), which were estimated using earlier $R_{BLR} - L_{5100}$ correlations also independents of $\dot{\mathcal{M}}$. The same figure also shows the distribution of the BH mass and the dimensionless accretion rate for the RM-selected sample (green, thin-barred histograms).

In summary, the sample consists of 55 AGN in the local Universe ($z < 0.3$) of which 19 have accurate estimations of $\dot{\mathcal{M}}$ and almost 60% (33/55) are accreting beyond $\dot{\mathcal{M}} \geq 3$. The objects in the latter group are the best candidates to host slim ADs. While incomplete, our sample is the largest and best of its kind, in particular in terms of a better definition of the BH mass and normalized accretion rate, and more uniform distribution of sources across the ranges of interest in these parameters.

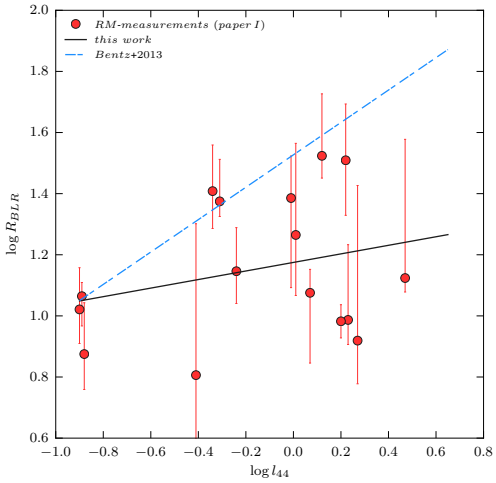

Figure 1. BLR size as a function of the optical luminosity at 5100Å (in units of 10^{44} erg/s) for the 16 fast accreging sources with RM-measurements that were presented in paper I (red points). The solid line represents the best-fit to this sample and corresponds to the relation assumed in this work. For comparison, we also show the best-fit relationship found for low Eddington ratio AGN (dashed line; Bentz et al. 2013).

3 DATA ANALYSIS

The IR to X-ray spectral properties of 16 out of 19 RM-selected AGN are presented in paper I. For each object, we reported observations from XMM-Newton that include simultaneous optical photometry and X-ray spectrum; and IR photometry from the most recent WISE All-Sky Data Release. The intrinsic AGN spectra were fitted with AD models in order to look for SED differences that depend on the dimensionless accretion rate $\dot{\mathcal{M}}$. The fitting took into account measured BH mass and accretion rates, BH spin (only two possibilities: $a = -1$ and $a = 0.998$), host-galaxy contribution, and intrinsic reddening of the sources. As shown in paper I, the primary AGN emission can be fitted by thin AD models over the range 0.2–1 μm regardless of the Eddington ratio. We see no evidence for extremely luminous ionizing continua, and no unusual torus emission (albeit the large aperture WISE data), in those sources expected to be powered by slim discs.

As of early 2015, only half of the reverberation mapped slim disc candidates had X-ray observations. Here we present, for the first time, X-ray observations of four RM-selected candidates to have slim AD (SDSS J075101.42+291419.1, SDSS J080101.41+184840.7, SDSS J081441.91+212918.5, and SDSS J100055.71+314001.2) that have been observed recently by XMM-Newton (PI: Shai Kaspi). These new AGN with the highest accretion rates $\dot{\mathcal{M}}>$ 20 were observed for the purpose of testing the slim-disc idea in the most extreme known cases. We follow the work of paper I to fit the IR-optical-UV SED of these RM-selected AGN (see Appendix A for a more explanations where the spectral analysis is presented). We found that the UV-optical SED of these four RM-selected AGN can also be fitted by thin AD models presenting moderate amount of reddening ($A_V \leq 0.4$). We also found that the soft X-ray emission, as well as the Comptonized power law, of these AGN with

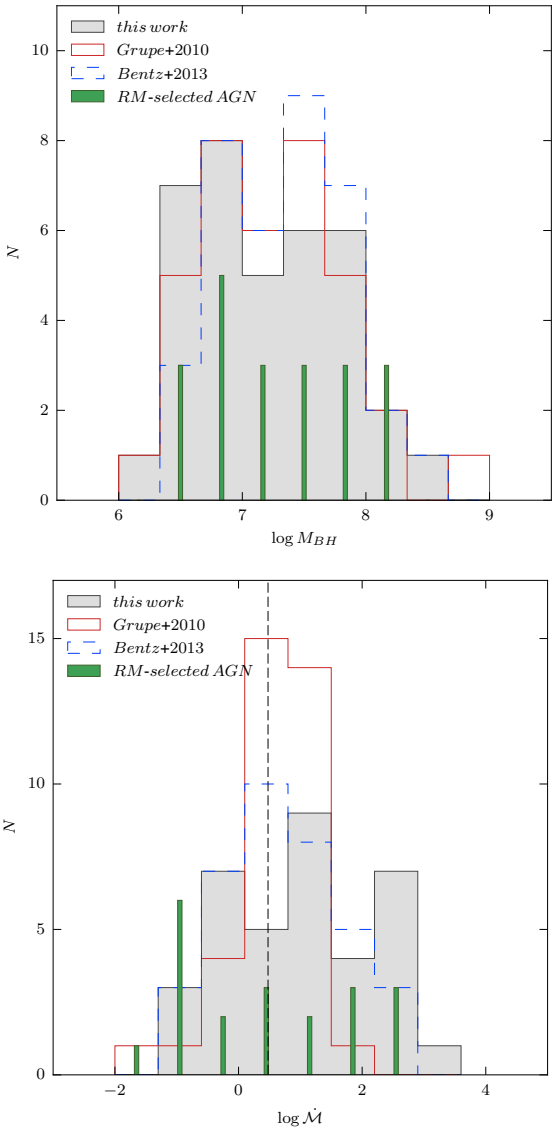

Figure 2. BH mass (top) and dimensionless accretion rate $\dot{\mathcal{M}}$ (bottom) for the RM-selected AGN (green, thin-barred histogram) and soft-X-ray-selected AGN samples used in this work (grey, step-filled histogram). The solid- and dashed-line distributions represent the distribution of the BH mass and the accretion rate of the soft-X-ray-selected AGN assuming the values given in Grupe et al. (2010) and those given by the $R_{BLR} - L_{5100}$ relationship for low accretion rate sources, respectively (Bentz et al. 2013). The vertical dashed-line in the bottom panel shows the empirical Eddington ratio threshold at $\dot{\mathcal{M}}$= 3 beyond which one needs to allow for the smaller BLR size for the same source luminosity.

the largest dimensionless accretion rate ($\dot{\mathcal{M}}$=20 – 200, are surprisingly similar to those from the parent sample ($\dot{\mathcal{M}}\geq$3) that have lower accretion rates. The spectral properties that were used in the correlation analysis for 16/19 RM-selected AGN are listed in paper I and those of the new 3/19 RM-selected AGN are presented in Table A3. As mentioned in the appendix, we were not able to carry out simultaneous optical spectrum for J080101 because of bad weather con-

ditions and we just used the results presented in paper I to derived its spectral properties.

The UV-optical-X-ray properties for the soft X-ray selected sample are taken from Grupe et al. (2010) based on simultaneous optical and X-ray observations. Their analysis focussed on finding differences between narrow and broad line Seyfert 1 galaxies. For each object, they reported observations from *Swift* that include simultaneous optical (UVOT photometry) and X-ray (XRT spectrum) observations. The optical/UV properties were determined from a single power-law model fit to the UVOT fluxes which account for possible host-galaxy contamination and Galactic extinction, as well as intrinsic reddening. The X-ray spectral properties were measured from the power-law fits to the XRT data. A summary of the X-ray and optical/UV properties for the soft-X-ray-selected AGN is given in Grupe et al. (2010).

Following paper I, we inferred the torus emission by fitting the most recent available WISE All-Sky Data Release for all the soft-X-ray-selected AGN. The torus SED was constructed from the four WISE bands, at 3.6, 4.5, 12, and 22 μm, using only data with a signal-to-noise ratio SNR>20. The observed infrared SED were modelled by the torus template of Mor & Netzer (2012) which is made of three components: a clumpy torus, a dusty narrow line region, and a hot pure-graphite dust component which represent the innermost part of the torus. We point the reader to paper I for a more detailed explanation of the fitting procedure. Similar to paper I, we find no evidence that the torus SED in fast accreting AGN is different from the one in slow accreting AGN. This means that either there is a very significant difference in the derived tours covering factors, with fast accreting AGN showing much smaller $L_{5\mu m}/L_{\rm AGN}$ by as much as an order of magnitude or, that our modelling of the UV continuum overestimates the real emission by a large factor (e.g. saturation). We return to this issue in the following section.

4 RESULTS AND DISCUSSION

4.1 Correlation Analysis

All spectral properties used in this paper are taken either from the spectral analysis presented in the works of Grupe et al. (2010), paper I or the analysis presented in Appendix A. We then explore the connection between the dimensionless accretion rate $\dot{\mathcal{M}}$, the X-ray and the infrared loudness[1] (α_{OX} and α_{IO}, respectively) in low-to-intermediate luminosity AGN, highlighting the slim AD candidates.

There are several fundamental differences between previous correlation analysis (Vasudevan & Fabian 2009; Grupe et al. 2010, and references therein) and this work. First, the BH mass estimated is based on a more realistic R_{BLR}–$L_{5100\text{Å}}$ relationship which leads to more accurate accretion rates. Second, the large number of sources per Eddington ratio interval, reduce the uncertainty due to variability of such sources especially at X-ray energies. Third, the correlation analysis is based on a Bayesian approach instead of a simple linear correlation analysis.

We adopted a new methodology to analyse the connection between the dimensionless mass accretion rate $\dot{\mathcal{M}}$ and the optical-to-X-ray spectral slope α_{OX} (see Section 4.2), as well as its connection with the IR-to-optical spectral slope α_{IO} (see Section 4.3). The paired parameters (e.g. α_{OX}–$\dot{\mathcal{M}}$) that represent a collection of individual measurements $\{(x_i, y_i)\}$ (e.g. $\{(\alpha_{OX_i}, \dot{\mathcal{M}}_i)\}$) is characterized by a two-step Bayesian approach. We use a Markov Chain Monte Carlo (MCMC)-based algorithm to study the "level" of correlation between both parameters and to characterize it.

First, we evaluate the degree of correlation between the two parameters by inferring the posterior probability density function (PDF) of the correlation coefficient assuming the following priors. The individual measurements (x_i, y_i) are independent with Gaussian distributed uncertainties and the distribution of the paired parameters is given by a bivariate normal distribution

$$\begin{array}{ccl} x_i & \mathcal{P}(x_i) & = \mathcal{N}(\mu_{x_i} = x_i, \sigma_{x_i} = 1/\delta^2_{x_i}) \\ y_i & \mathcal{P}(y_i) & = \mathcal{N}(\mu_{y_i} = y_i, \sigma_{y_i} = 1/\delta^2_{y_i}) \\ (x_i, y_i) & \mathcal{P}(x_i, y_i) & = \mathcal{N}(\mu(\mu_{x_i}, \mu_{y_i}), \Sigma(\sigma_{x_i}, \sigma_{y_i}, \rho)) \end{array}$$

where δ_{x_i} and δ_{y_i} are the measured uncertainties on x_i and y_i, respectively; and ρ is the correlation coefficient with a uniform prior distribution defined between -1 (anti-correlated with no scatter) and +1 (correlated with no scatter).

For those cases that show signs of correlation, we characterize the parameters that govern such correlation through modelling the collection of individual measurements $\{(x_i, y_i)\}$ with three different functional forms: a line

$$f(x) = \beta x + \alpha_0 \tag{4}$$

a broken power-law

$$f(x) = \begin{cases} \alpha_0 & x < \dot{\mathcal{M}}_c \\ \alpha_0 + \beta \log \frac{x}{\dot{\mathcal{M}}_c} & x \geq \dot{\mathcal{M}}_c \end{cases} \tag{5}$$

and a sigmoid given by

$$f(x) = \alpha_0 + \frac{\Delta\alpha_0}{1 + e^{-\beta \log \frac{x}{\dot{\mathcal{M}}_c}}} \tag{6}$$

Assuming also independence between the individual measurements and Gaussian distribution for their uncertainties, we infer the posterior PDF of each model parameter: $\{\alpha_0, \beta\}$, $\{\alpha_0, \beta, \dot{\mathcal{M}}_c\}$ or $\{\alpha_0, \Delta\alpha_0, \dot{\mathcal{M}}_c, \beta\}$ (for the line, the broken power-law and the sigmoid function, respectively) assuming that

$$y_i = f(x_i) + \mathcal{N}(\mu = y_i, \sigma = 1/\delta^2_{y_i}).$$

After testing for several possible priors (Gaussian, Exponential and Uniform probabilities), we found that the posterior PDF of the model's parameter is insensitive to its prior distribution. Finally, once the posterior PDFs are inferred (i.e. the model is fitted), we evaluate the goodness of the fit through the statistic p which uses the Freeman-Turkey criterion. Using the model's parameter posterior PDFs, we generate a family of N "expected values" (and hence a family of N simulated values), to infer the probability distribution of the difference between both the observed and simulated

[1] The X-ray loudness is defined as the optical-to-X-ray spectral slope $\alpha_{OX} = -0.3838 \log \left[\frac{L_\nu(2\text{keV})}{L_\nu(2500\text{Å})}\right]$ (Tananbaum et al. 1979)

Table 1. BH mass, intrinsic dimensionless accretion rates and the logarithm of the corrected monochromatic luminosities at 2 keV, 2500Å, 5100Å and 5μm in units of erg s^{-1}. The first block represents sources with RM results, while the second block corresponds to the soft-X-ray-selected AGN sample (see Sect. 2).

Object	z	$\log \frac{M_{BH}}{M_\odot}$	$\log \dot{\mathcal{M}}$	$\log \frac{L_{2\,\mathrm{keV}}}{\mathrm{erg/s}}$	$\log \frac{L_{2500\text{Å}}}{\mathrm{erg/s}}$	$\log \frac{L_{5100\text{Å}}}{\mathrm{erg/s}}$	$\log \frac{L_{5\mu\mathrm{m}}}{\mathrm{erg/s}}$
SDSS J075101.42+291419.1†	0.121	7.16	1.34	41.67	44.70	44.48	44.29
SDSS J080101.41+184840.7	0.140	6.78	2.53	43.49	44.98	44.27	44.51
SDSS J081441.91+212918.5	0.163	6.97	1.64	43.68	44.53	44.01	44.02
SDSS J100055.71+314001.2	0.195	6.50	1.90	43.45	44.54	44.12	44.34
SDSS J093922.89+370943.9	0.186	6.53	2.65	43.28	44.63	44.07	44.47
Fairall 9	0.047	8.09	-0.70	43.63	44.60	43.98	44.57
IRAS F12397+3333	0.044	6.79	2.94	43.23	44.51	44.23	43.82
PG 0844+349	0.064	7.66	0.82	43.52	44.69	44.22	44.17
PG 2130+099	0.063	7.05	1.75	43.23	44.75	44.20	44.62
PG 1229+204	0.063	8.03	-1.04	43.43	44.23	43.70	44.09
Mrk 817	0.031	7.99	-0.88	43.19	44.12	43.74	44.14
Mrk 279	0.030	7.97	-0.86	43.40	44.15	43.71	43.69
Mrk 290	0.029	7.55	-0.82	42.85	43.89	43.17	43.58
Mrk 79	0.022	7.84	-0.60	42.39	43.79	43.68	43.86
Mrk 1511	0.034	7.29	-0.35	42.84	43.64	43.16	43.48
Mrk 590	0.026	7.55	-0.28	42.65	43.59	43.50	43.39
Mrk 110	0.035	7.10	0.85	43.63	44.35	43.66	43.76
Mrk 382	0.033	6.50	1.20	42.84	43.65	43.12	43.22
Mrk 335	0.026	6.93	1.39	43.31	44.29	43.76	43.97
RX J2301.6-5913	0.149	8.48	-1.07	44.07	44.36	44.27	44.67
RX J1413.6+7029	0.107	7.80	-0.27	43.41	43.54	43.89	44.03
RX J0311.3-2046	0.070	7.85	-0.20	43.41	44.19	44.00	44.18
RX J0437.4-4711	0.052	7.75	-0.06	43.20	44.04	43.97	43.87
RX J0100.4-5113	0.062	7.57	0.34	43.08	44.10	44.00	44.19
RX J0319.8-2627	0.076	7.60	0.43	43.02	44.21	44.09	43.94
RX J2146.6-3051	0.075	7.54	0.44	43.15	44.17	44.02	44.00
RX J0105.6-1416	0.070	7.18	1.26	43.51	44.16	44.09	44.14
RX J0859.0+4846	0.083	7.34	1.30	43.48	44.62	44.32	44.26
RX J0128.1-1848	0.046	7.18	1.15	43.37	44.04	44.01	43.90
RX J1007.1+2203	0.083	6.61	1.64	42.53	43.65	43.58	43.68
RX J2258.7-2609	0.076	6.99	1.91	43.13	44.30	44.27	43.89
RX J2242.6-3845	0.221	6.96	2.27	43.67	44.61	44.47	44.51
RX J2217.9-5941	0.160	6.67	2.40	42.84	44.32	44.17	44.68
RX J1355.2+5612	0.122	6.44	2.82	43.18	44.30	44.14	44.16
RX J2317.8-4422	0.132	6.36	2.85	42.96	44.16	44.05	44.06
RX J1304.2+0205	0.229	6.63	2.88	43.39	44.58	44.43	44.72
RX J1319.9+5235	0.092	6.30	2.97	42.81	44.24	44.06	43.68
Mrk 493	0.032	6.11	2.84	42.25	43.79	43.71	43.63
Mrk 684	0.046	6.54	2.41	42.94	44.11	44.00	43.82
Mrk 841	0.036	8.00	-0.86	43.07	43.95	43.77	43.93
Mrk 1048	0.042	8.11	-0.63	43.44	44.30	44.07	44.20
Mrk 141	0.042	7.53	0.01	42.77	43.49	43.72	43.69
Mrk 142	0.045	6.70	1.48	42.84	43.72	43.60	43.62
AM 2354-304	0.033	7.05	0.80	42.70	43.56	43.60	43.41
MS 2254-36	0.039	6.66	1.65	42.82	43.81	43.66	43.80
NGC 4593	0.009	7.81	-0.52	41.51	43.44	43.74	43.11
Fairall 1119	0.055	7.70	-0.41	43.15	43.31	43.66	43.73
Fairall 1116	0.059	7.88	-0.15	43.25	44.26	44.08	44.37
Fairall 303	0.040	6.58	1.45	42.79	43.62	43.42	43.40
Ton 730	0.087	7.61	0.20	43.40	44.36	43.96	44.05
CBS 126	0.079	7.30	1.02	43.07	44.35	44.09	44.03
ESO 301-G13	0.059	7.08	1.10	43.18	43.96	43.85	44.08
EXO 1627+40	0.272	6.70	2.52	44.11	44.50	44.29	44.54
KUG 1618+410	0.038	6.80	1.19	42.21	43.64	43.53	43.05
VCV 0331-37	0.064	6.85	1.41	43.06	43.94	43.75	43.34

†The short X-ray exposure time does not allow to obtain good quality spectra above 3 keV.

to the expected values. On average we expected the difference between them to be zero; hence, p is simply the fraction of simulated discrepancies that are larger than their corresponding observed discrepancies. Therefore, if p is very large ($p > 0.975$) or very small ($p < 0.025$) the model is not consistent with the data.

Throughout this work, the listed value for the correlation coefficient ρ, the model's parameter and the goodness of the fit p correspond to the most likely value according to its posterior PDF, and the errors represents the $2.5^{\rm th}$ and $97.5^{\rm th}$ percentiles of that probability.

4.2 X-ray loudness, α_{OX}

We applied the method, presented in the previous section, to analyse the connection between the X-ray loudness, α_{OX}, and $\dot{\mathcal{M}}$.

Some correlations between α_{OX} and other spectral properties have been reported. While, it is widely accepted that α_{OX} correlates with the X-ray bolometric correction factor and the hard X-ray photon index (Vasudevan et al. 2009; Marchese et al. 2012; Jin et al. 2012), a possible correlation between α_{OX} with the Eddington ratio is still under debate. Some earlier studies (Vasudevan et al. 2009; Fanali et al. 2013; Plotkin et al. 2016) report a lack of a correlation between α_{OX} and $\dot{m}$, but Grupe (2011) claim that they are strongly correlated. Most important, perhaps, is the ability to separate those correlations linking α_{OX} to source luminosity, over a large luminosity range (e.g. Vasudevan & Fabian 2009; Grupe 2011) from those comparing α_{OX} with the normalized accretion rate. To understand the nature of slim AD systems, we will focus solely on the correlation with $\dot{\mathcal{M}}$. Our main concern is to explore whether the fast accreting systems follow the same connection between α_{OX} and $\dot{\mathcal{M}}$ over a limited range of luminosities. We note, again, that in our sample we can only constrain $L_{5100\text{Å}}$, not Lbol.

After re-estimating the BH mass, and hence the Eddington ratio, by assuming the new dependence of R_{BLR} on $L_{5100\text{Å}}$ (section 2.1), and adding accurate measurements of the accretion rate (RM-selected AGN), we find that α_{OX} is *weakly correlated* with $\dot{\mathcal{M}}$ ($\rho = 0.31^{+0.20}_{-0.25}$). As we can see in the Fig. 3, the high Eddington ratio tail, i.e. $\dot{\mathcal{M}} \gtrsim 10$, displays the larger spread in α_{OX} and appears to be slightly shifted to higher values. When the sample is limited to those AGN that are accreting below $\dot{\mathcal{M}} < 10$ (28/59) the analysis shows a lack of correlation ($\rho = -0.04^{+0.37}_{-0.36}$). This suggests that the *weak* α_{OX}-$\dot{\mathcal{M}}$ *correlation* is dominated by the fast accreting AGN. Indeed, when the sample is limited to those AGN that are accreting beyond $\dot{\mathcal{M}} \geq 10$ (31/59), we find that α_{OX} is strongly correlated with $\dot{\mathcal{M}}$ with $\rho = 0.42^{+0.10}_{-0.11}$. This results confirms what it is usually found in the literarue, i.e. the X-ray loudness does not correlate with the dimensionless accretion rate. This result is at odds with that of Grupe (2011) who find a strong correlation between the X-ray loudness and the Eddington ratio. However, the Eddington ratio derived by Grupe (2011) are based on the bolometric luminosity as given by the best-fit power-law model to simultaneous X-ray spectra and UVOT photometry which introduces a non-systematic error on the inferred Eddington ratio.

Our approach to this dependence is different and assumes that α_{OX} is different in low and high accretion rate

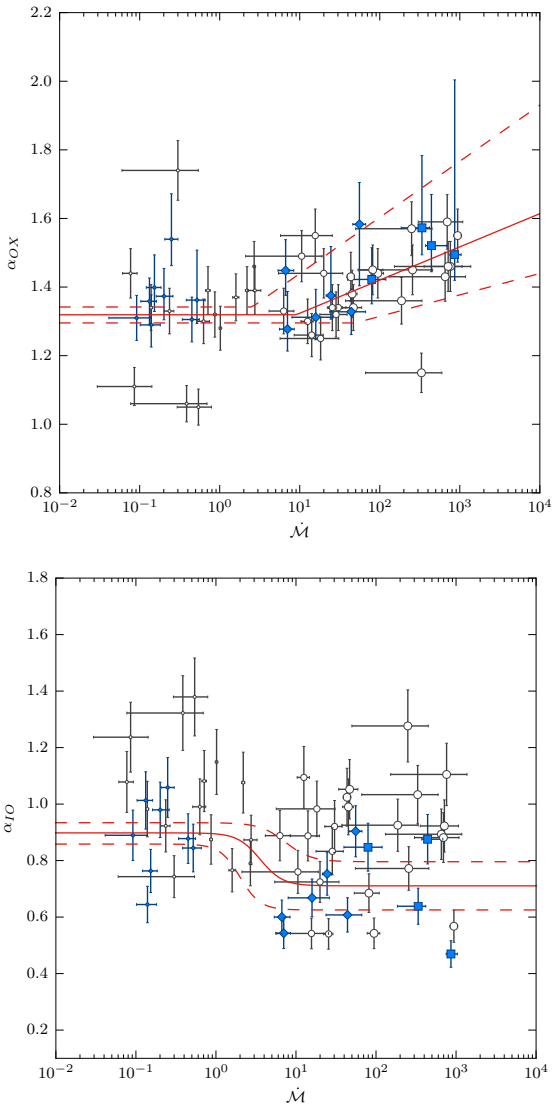

Figure 3. X-ray (α_{OX}) and IR (α_{IO}) loudness as a function of the Eddington ratio for both RM-selected AGN sample (blue, filled diamonds) and soft-X-ray-selected AGN sample (grey, empty circles). The symbol size scales with the mass accretion rate bins: $\dot{\mathcal{M}}$<3.0, 3.0 $\leq\dot{\mathcal{M}}<\dot{\mathcal{M}}_{min}$, and $\dot{\mathcal{M}}\geq\dot{\mathcal{M}}_{min}$. The diagrams show our best fit model for the two correlations, a broken power law at the top and a sigmoid function at the bottom.

AGN and that there is a smooth transition between these value which may be related to some new physics (e.g. the onset of slim disc accretion). We modelled the dependence of α_{OX} on the accretion rate $\dot{\mathcal{M}}$ by fitting a broken power law (Eq. 5), as well as a sigmoid function (Eq. 6), to the data. Both models give satisfactory fit to the data but the broken power law is slightly better and hence is used for the rest of the analysis. Fig. 3 shows our determination for the transition accretion rate ($\dot{\mathcal{M}}_c$ in Eq. 5), the most likely α_{OX} for low accreting sources (α_0 in Eq. 5) and the transition between low and high α_{OX} regime which is regulated by the parameter β in Eq. 5. As shown in Fig. 4, the model's parameters ($\dot{\mathcal{M}}_c$, α_0 and β) are well constrain. The posterior probability density gives a transi-

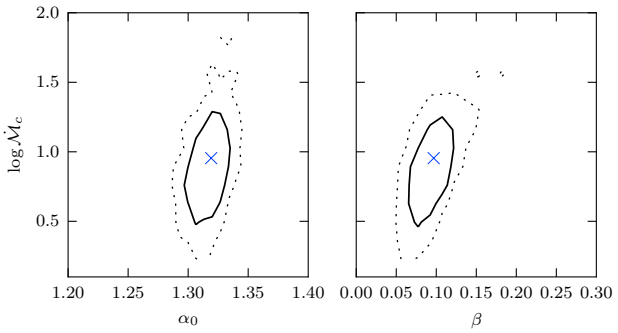

Figure 4. The 68 percent and 95 percent confidence intervals from the MCMC analysis of α_{OX}–$\dot{\mathcal{M}}$. Contours show the constraints on the transition accretion rate with both the most likely α_{OX} for low accreting AGN (*left*) and the right side shows the best β in the broken power-law model. The cross point to the most likely value of each model's parameter.

tion accretion rate of $\dot{\mathcal{M}}_c = 8.9^{+40.0}_{-6.4}$ and a X-ray loudness of $\alpha_{OX} = \alpha_0 = 1.32^{+0.02}_{-0.03}$ for objects that are accreting below $\dot{\mathcal{M}}$<$\dot{\mathcal{M}}_c$ which is significantly lower than the most likely value for the highest accretion rates α_{OX}= $1.49^{+0.05}_{-0.05}$. We also tried to fit the data with a line, with no transition point, but that did not result in a satisfactory fit, $p = 0.015$.

While the uncertainty on the preferred value of the transition accretion rate is large, because of the small number of objects and the large uncertainties on the accretion rate, it is clear that the value obtained from fitting our sample is considerably lower than $\dot{\mathcal{M}}_c$ =50 preferred by Mineshige et al. (2000), but consistent with $\dot{\mathcal{M}}_c$ =20 suggested by Watarai et al. (2001). The transition accretion rate found here is also consistent with those found by Du et al. (2015) and Du et al. (2016b), which are also based on observational constrains ($\dot{\mathcal{M}}_c = 13.8^{+19.6}_{-8.1}$ and $\dot{\mathcal{M}}_c = 11.19^{+2.29}_{-6.22}$, respectively). The minimum accretion rate of $\dot{\mathcal{M}}_{min}$=3 used by us to define slim AD candidates is within the error bar, but at the lower end of the confidence level. As pointed out in Du et al. (2015), there must be a smooth transition from thin to slim discs and, wherefore, relatively large range in $\dot{\mathcal{M}}$ from flat to linear dependence on $\dot{\mathcal{M}}$.

4.3 Infrared loudness, α_{IO}

The re-emitted IR radiation can also be used as a proxy of the primary nuclear emission. In this section we use the IR (torus) emission to carry an analysis of the optical-IR relation, similar to the UV-X-ray relation discussed in the previous section. Figure 3 shows the dependence on the dimensionless accretion rate of the IR loudness which is defined as the infrared-to-optical spectral slope

$$\alpha_{IO} = -0.7687 \log \frac{L_\nu(2500\text{Å})}{L_\nu(5\mu\text{m})}. \quad (7)$$

In contrast to the X-ray loudness, we find that there is no correlation between α_{IO} and $\dot{\mathcal{M}}$ when the sample is split into lower ($\dot{\mathcal{M}}$< 10) and higher ($\dot{\mathcal{M}}\geq$ 10) mass accreting AGN ($\rho \sim 0$). However, when the whole sample is considered we find a weak correlation ($\rho = -0.25^{+0.22}_{-0.09}$). As we can see in Figure 3, those sources accreting beyond $\dot{\mathcal{M}}_{min}$ appear to be shifted to lower α_{IO} values. We modelled the correlation by fitting the data to a sigmoid function (Eq. 6). This enables us to determine the transition accretion rate ($\dot{\mathcal{M}}_c$ in Eq. 6), as well as the most likely α_{IO} for low (α_0 in Eq. 6) and high ($\alpha_0 + \Delta\alpha_0$ in Eq. 6) accretion rate AGN. We found that the transition accretion rate is consistent with that given by the α_{OX}–$\dot{\mathcal{M}}$ correlation ($\dot{\mathcal{M}}_c = 3.6^{+5.0}_{-1.2}$). The posterior probability density gives an IR loudness of α_{IO}= $\alpha_0 = 0.91^{+0.03}_{-0.04}$ for objects that are accreting below $\dot{\mathcal{M}}$<$\dot{\mathcal{M}}_c$ and a shift between low and high accreting AGN of $\Delta\alpha_0 = -0.19^{+0.04}_{-0.05}$. This means that for a given UV monochromatic luminosity, the torus luminosity appear to be slightly lower for high accreting AGN (see Figure 5).

4.4 Median SED

Fig. 5 shows the median primary AGN and torus SED normalized at 2500Å for two ranges: $\dot{\mathcal{M}}$<$\dot{\mathcal{M}}_{min}$ and $\dot{\mathcal{M}}\geq\dot{\mathcal{M}}_{min}$ ($\dot{\mathcal{M}}_{min}$=3; solid and dashed lines, respectively). The median primary AGN SED was constructed from the best-fitted thin AD models to the RM-selected sample. To construct the median torus SED we used the best-fitted torus templates of the entire sample (i.e. RM- and soft-X-ray-selected samples). The four straight lines represent the median optical-to-X-ray and IR-to-optical spectral slopes (note that the diagram shows νL_ν and the spectral slopes -α_{OX}, α_{IO}- are defined through monochromatic luminosities). In general, the torus and the disc corona in the fastest accreting systems, i.e. $\dot{\mathcal{M}}\gtrsim$10, are less efficient in reprocessing the primary AGN radiation having (i.e. higher α_{OX} and lower α_{IO}).

In paper I, we found a relatively low ratio of total AGN luminosity, produced mostly in the UV part of the disc SED, and the reprocessed radiation by the torus for fast accreting systems, $L_{torus}/L_{AGN} \sim 10^{-1} - 10^{-2}$. This ratio is not too different from the one predicted by several theoretical estimates (Kawakatu & Ohsuga 2011) which take into account both the saturated luminosity of the slim disc and the strong angular dependence of the emitted radiation. However, the surprising similarity of $L_{5100\text{Å}}/L_{torus}$ in AGN with slow and fast accretion rates (thin and slim ADs) suggests either a fine tuning of the parameters or some wrong assumptions about the physics of slim ADs. The IR loudness measured here, which shows how the torus of fast accreting systems are less efficient in reprocessing the emitted intrinsic AGN radiation, is a manifestation of this issue.

A simple way to appreciate this difficulty is to note that the bolometric correction factor at $L_{5100\text{Å}}$ is very different for thin and slim ADs even when saturation is taken into account. This is illustrated in Fig. 6 of paper I where we show this correction factor to be about 10 for thin ADs and 100 or more for slim discs. Thus a certain $L_{5100\text{Å}}$ will indicate a slim disc luminosity which is at least an order of magnitude larger than the one for a thin disc. However, the uniform α_{IO} we measure suggest that $L_{torus}/L_{5100\text{Å}}$ is basically identical for both groups. This would mean that either the torus geometrical covering factor in systems powered by slim ADs is 10 times or more smaller, or that the angular dependence of the emitted SED is such that, compared with thin disc systems, the torus observed only 10% of the emitted radiation. At first, this by itself seemed to be unlikely because it requires such fine tuning. However the inclusion

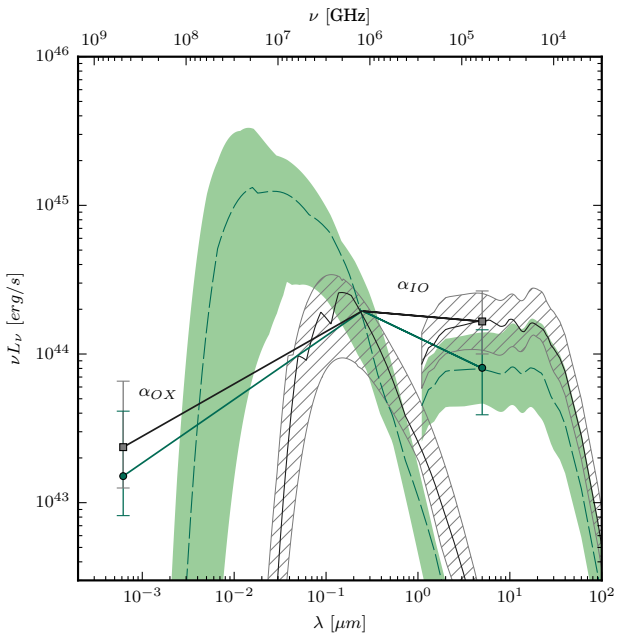

Figure 5. Median AGN SEDs normalized at 2500Å for the two groups: green, dashed line represents sources accreting at $\dot{\mathcal{M}} \geq \dot{\mathcal{M}}_{min}$, and black, solid line sources accreting at $\dot{\mathcal{M}} < \dot{\mathcal{M}}_{min}$. The dashed areas show the 25^{th} and 75^{th} percentiles. The square ($\dot{\mathcal{M}} < \dot{\mathcal{M}}_{min}$) and circle ($\dot{\mathcal{M}} \geq \dot{\mathcal{M}}_{min}$) points represent the median luminosity at 2keV and 5 μm. For each Eddington ratio bin, there are two *horitzontal* lines that represents α_{OX} and α_{IO}.

of self-shadowing effects and/or highly energetic winds in slim AD, which must dramatically affect the re-emitted IR emission, might help to make such fine tuning possible.

5 CONCLUSIONS

We conducted an investigation of various spectral properties in two AGN samples covering a limited luminosity range. The RM measurements and the new estimates of R_{BLR} introduced here, allow the most accurate BH mass estimates, and hence Eddington ratios. We implemented a Bayesian approach which enables us to infer the posterior probability density of the correlation coefficient (ρ) used to evaluate the degree of correlation between two spectral properties, α_{OX} and α_{IO}, and the dimensionless accretion rate of the sources, $\dot{\mathcal{M}}$. The main results of our study can be summarized as follows:

(i) The optical-to-UV SED of all sources, including those with the highest mass accretion rates ($\dot{\mathcal{M}}$>20), can be fitted with thin AD models, as claimed in our previous work (paper I).

(ii) We do not find any correlation between the X-ray loudness (α_{OX}) and the dimensionless accretion rate ($\dot{\mathcal{M}}$), up to a very large value of $\dot{\mathcal{M}}_{min} \sim 10$. However, the highest Eddington ratio ($\dot{\mathcal{M}} \geq \dot{\mathcal{M}}_{min}$) sources appear to show systematically larger values of α_{OX}. The correlation claimed in earlier works which extends to much lower Eddington ratios is due to a small number of very large $\dot{\mathcal{M}}$ sources that were compared with low $\dot{\mathcal{M}}$ sources, as well as to an inaccurate estimation of the mass accretion rate.

(iii) We defined a new IR-to-optical spectral index, α_{IO}, which is a measure of the reprocessing efficiency of the central torus. We found that the distribution of α_{IO} of the highest Eddington ratio group appear to be shifted to lower values. This finding seems to contradict several of the assumptions used to obtain the good fit to the observed SEDs in most of the sources. We suggest that additional physical processes that act to reduce the extreme UV radiation are at work in fast accreting AGN related to photon trapping, strong winds, and perhaps other yet unknown physics processes. The alternative explanation, which we consider unlikely, is extremely small covering factor for high $\dot{\mathcal{M}}$ sources (see Castelló-Mor et al. 2016).

Our new results, failing to recover the predicted differences between the SEDs of slim and thin ADs, within the extensive wavelength range considered here, hint to a sever problem in present slim AD theoretical models. Additional physics, occurring in the nuclear regions of high accreting AGN and responsible for making the SED of slim ADs consistent with that of thin discs, must be at work. One such process could be powerful winds as slim AD simulations suggests. In this scenario winds are responsible for carrying away a significant amount of the energy from the inner-most region of the AD, decreasing its radiation in the UV part of the spectrum, in particular the UV ionizing radiation responsible for high excitation emission lines, as well as reduce the Comptonized emission or perhaps quenching the disc corona. This will allow reconciliation of our observations (IR/optical/UV/X-ray) with slim disc theory and simulations. If such winds originating in the innermost part of the slim disc they can affect the dusty torus structure in a way which is different from what is known in slow accreging systems. Such an effect has never been investigated.

ACKNOWLEDGEMENTS

We would like to thank the referee, Chris Done, for helpful comments that greatly improved the clarity of the paper. Funding for this work has been provided by a joint ISF-NSFC grant number 83/13. HN acknowledges the support of ISSI during a work meeting in 2015. LCH acknowledges support from the Chinese Academy of Science (grant No. XDB09030102), National Natural Science Foundation of China (grant No. 11473002), and Ministry of Science and Technology of China (grant No. 2016YFA0400702). Bian W.H. thanks the support from the National Science Foundations of China (No. 11373024).

REFERENCES

Abramowicz M. A., Czerny B., Lasota J. P., Szuszkiewicz E., 1988, ApJ, 332, 646
Bentz M. C., Peterson B. M., Netzer H., Pogge R. W., Vestergaard M., 2009, ApJ, 697, 160
Bentz M. C., et al., 2013, ApJ, 767, 149
Cardelli J. A., Clayton G. C., Mathis J. S., 1989, ApJ, 345, 245
Castelló-Mor N., Netzer H., Kaspi S., 2016, MNRAS, 458, 1839
Charlot S., Bruzual A. G., 1991, ApJ, 367, 126
Collin S., Kawaguchi T., 2004, A&A, 426, 797

Dietrich M., Hamann F., Shields J. C., Constantin A., Vestergaard M., Chaffee F., Foltz C. B., Junkkarinen V. T., 2002, ApJ, 581, 912
Du P., et al., 2014, ApJ, 782, 45
Du P., et al., 2015, ApJ, 806, 22
Du P., et al., 2016b, ApJ, 825, 126
Du P., et al., 2016a, ApJ, 825, 126
Fanali R., Caccianiga A., Severgnini P., Della Ceca R., Marchese E., Carrera F. J., Corral A., Mateos S., 2013, MNRAS, 433, 648
Frank J., King A., Raine D. J., 2002, Accretion Power in Astrophysics: Third Edition
Gordon K. D., Clayton G. C., Misselt K. A., Landolt A. U., Wolff M. J., 2003, ApJ, 594, 279
Grupe D., 2011, in Narrow-Line Seyfert 1 Galaxies and their Place in the Universe. p. 4 (arXiv:1106.0228)
Grupe D., Komossa S., Leighly K. M., Page K. L., 2010, ApJS, 187, 64
Jiang Y.-F., Stone J. M., Davis S. W., 2014, ApJ, 796, 106
Jin C., Ward M., Done C., 2012, MNRAS, 425, 907
Kaspi S., Smith P. S., Netzer H., Maoz D., Jannuzi B. T., Giveon U., 2000, ApJ, 533, 631
Kawakatu N., Ohsuga K., 2011, MNRAS, 417, 2562
Laor A., Netzer H., 1989, MNRAS, 238, 897
Marchese E., Della Ceca R., Caccianiga A., Severgnini P., Corral A., Fanali R., 2012, A&A, 539, A48
Mineshige S., Kawaguchi T., Takeuchi M., Hayashida K., 2000, PASJ, 52, 499
Mor R., Netzer H., 2012, MNRAS, 420, 526
Netzer H., 2013, The Physics and Evolution of Active Galactic Nuclei
Plotkin R. M., Gallo E., Haardt F., Miller B. P., Wood C. J. L., Reines A. E., Wu J., Greene J. E., 2016, preprint, (arXiv:1605.00742)
Sądowski A., Narayan R., 2016, MNRAS, 456, 3929
Sądowski A., Abramowicz M., Bursa M., Kluźniak W., Lasota J.-P., Różańska A., 2011, A&A, 527, A17
Shakura N. I., Sunyaev R. A., 1973, A&A, 24, 337
Slone O., Netzer H., 2012, MNRAS, 426, 656
Tananbaum H., et al., 1979, ApJ, 234, L9
Vasudevan R. V., Fabian A. C., 2009, MNRAS, 392, 1124
Vasudevan R. V., Mushotzky R. F., Winter L. M., Fabian A. C., 2009, MNRAS, 399, 1553
Vasudevan R. V., Brandt W. N., Mushotzky R. F., Winter L. M., Baumgartner W. H., Shimizu T. T., Schneider D. P., Nousek J., 2013, ApJ, 763, 111
Wang J.-M., Zhou Y.-Y., 1999, ApJ, 516, 420
Wang J.-M., Du P., Valls-Gabaud D., Hu C., Netzer H., 2013, Physical Review Letters, 110, 081301
Wang J.-M., et al., 2014, ApJ, 793, 108
Watarai K.-y., Mizuno T., Mineshige S., 2001, ApJ, 549, L77
Woo J.-H., Yoon Y., Park S., Park D., Kim S. C., 2015, ApJ, 801, 38
Zhou X.-L., Zhang S.-N., 2010, ApJ, 713, L11

APPENDIX A: NEW SIMULTANEOUS BROADBAND SED

The following is a detailed spectral analysis of four SEAMBHs with the highest Eddington ratio up to now (SDSS J075101.42+291419.1, SDSS J080101.41+184840.7, SDSS J081441.91+212918.5, and SDSS J100055.71+314001.2) that have been recently observed with XMM-Newton. The structure of this appendix is as follows: the new X-ray observations are described in Sect. A1; the optical-to-UV SED is presented in Sect. A2; finally, the X-ray spectral analysis, as well as the principal conculsions are discussed in Sect. A3.

A1 New XMM-Newton Observations

The sources J075101, J080101, J081441 and J100055 were observed with XMM-Newton between May and October of 2015. During all the observations, the European Photon Imaging Cameras (EPIC) pn and MOS were operated in full window mode. The observation data files (ODFs) were processed following the standard procedures to produce calibrated event lists using the Science Analysis System (SAS 14.0.0). We defined the source extraction region to be circular with radii ranging from 30″ to 35″ centred on the bright pixel closer to the optical source position. We used single- and double-pixel events for all observations. The background was selected from nearby circular regions free of sources and preferentially on the same CCD chip. Spectral response files were generated using the SAS tasks RMFGEN and ARFGEN. The EPATPLOT SAS task was used to test for the presence of pile up. The EPIC X-ray spectra of all the observations were found to be free from the effects of pile-up.

The sources were also observed with the Optical Monitor (OM) abroad of XMM-Newton, providing us with optical to UV photometry simultaneously to the EPIC observations. These observations were reduced using the OMICHAIN pipeline. Point source and extended source identification is automatically performed as part of this pipeline, and the point source corresponding to the nucleus was selected using the images generated for each waveband, ensuring that the identified optical or UV counterpart was coincident with the source region used for the X-ray spectrum. The optical/UV photometry results were extracted from the SWSRLI results files. To prepare the OM data, the *om_filter_default.pi* file and all response files for the U, UVW1, UVM2, UVW2 filters were downloaded from the OM response file directory in HEASARC Archive[2]. Each count rate and its associated error were entered into the default filter file and then combined with the response file of the corresponding OM filter, again by using the GRPPHA tool to produce OM data that could be used in XSPEC.

We were also able to carry out simultaneous optical observations from the Lijiang 2.4m for three of the four RM-selected SEAMBHs (J075101, J081441 and J100055). The observations were done as close as possible in time to the XMM-Newton observations, as much as weather and telescope time limitations permitted (see Table A1 for dates). Due to bad weather conditions J080101 was not observed. The observation and the reduction of the optical spectra followd the standard technique that is described in **?**. This procedure resulted with flux calibrated optical spectra.

The XMM-Newton EPIC spectra are combined with the optical/UV photometry and optical spectroscopy to construct a simultaneous broadband nuclear SED for each AGN. There is an ubiquitous data gap in the far UV region due to absorption by Galactic gas and dust. Since the intrinsic SED for our low-redshift, low-BH mass AGN peaks in this band, it is very difficult to estimate the bolometric luminosity and hence the spin of the BH (see paper I).

[2] http://heasarc.gsfc.nasa.gov/FTP/xmm/data/responses/om/

Table A1. Information on the observed source and observations.

Object SDSS ...	z	RM results $\log M_{BH}$ [$M\odot$]	RM results $\log \dot{\mathcal{M}}$	RM results $\log L_{5100\text{Å}}$ [erg s^{-1}]	$E(B-V)$ Galactic	EPIC pn date	EPIC pn t [ks]	EPIC pn CR [cts]	Lijiang date
J075101.42+291419.1†	0.1208	$7.16^{+0.17}_{-0.09}$	$1.34^{+0.25}_{-0.41}$	44.48	0.042	2015-05-04	10.65	244	2015-05-04
J080101.41+184840.7	0.1396	$6.78^{+0.34}_{-0.17}$	$2.33^{+0.39}_{-0.72}$	45.01	0.032	2015-10-10	21.35	38985	*a*
J081441.91+212918.5	0.1628	$6.97^{+0.23}_{-0.27}$	$1.56^{+0.63}_{-0.57}$	44.65	0.039	2015-10-15	12.22	23233	2015-10-19
J100055.71+314001.2‡	0.1948	$6.50^{+0.20}_{-0.20}$	$1.90^{+0.50}_{-0.50}$	44.12	0.017	2015-06-02	18.27	8477	2015-06-01

†The short exposure time does not allow to obtain good quality spectra above ∼3 keV.

‡ The Hβ lag was consistent with zero, so the BH mass and the accretion were estimated using the correlation between the BH mass and $L_{5100}^{1/2}FWHM^2$, see Sect. 2.1.

*a*The object J080101 was not observed due to bad weather conditons.

A2 Fitting thin AD models

For the three RM-selected AGN with new simultaneous optical and X-ray observations (J075105, J081441 and J100055) we fitted thin AD models to the new simultaneous observations following the methodology discussed in paper I. We correct for Galactic extinction, subtracted the stellar and emission line contributions, and considered the possibility of intrinsic reddening of the sources. For the Galactic interstellar reddening, we assumed the Cardelli et al. (1989) extinction law using the Galactic extinction colour excess $E(B-V)$ obtained from the NASA/IPAC Infrared Science Archieve[3]. The most consistent approach for the intrinsic reddening is to add this as a free parameter in the disc modelling analysis. The narrow spectral window of our data makes it impossible to distinguish between different extinction curves, so the intrinsic reddening were modelled by a SMC extinction-like curve (Gordon et al. 2003) that best represents typical type-I AGN. The host-galaxy contribution was estimated using the fact that the broad Hβ lines show no Baldwin effect (Dietrich et al. 2002). This means that the observed equivalent width of the line, EW(Hβ), can be used to derive the fraction of the non-AGN light entering the aperture at 4861Å. We used an average EW(Hβ) of (89 ± 31)Å which is representative of SEAMBHs (Du et al. 2015).

We used the Slone & Netzer (2012) code to calculate a large number of thin disc spectra that include the entire range of BH mass and accretion rate expected in our sample. The fitting procedure includes the comparison of the observed SED with various combination of disc SEDs covering the range of mass, accretion rate and intrinsic reddening. The reddening is taken into account by changing $E(B-V)$ in steps of 0.004 mag, calculating, for each value, a new mass accretion rate and its range of uncertainty. A simple χ^2 procedure was used to find the best-fit combination of reddening and thin AD models. We use three line-free windows covering the optical spectroscopic data, and the simultaneous OM photometry. The line-free windows are centred on 4205Å, 5100Å and 6855Å, with widths ranging from 10 to 30Å. For the error on each continuum point, we combine the standard error from the Poison noise, an assumed 5% error on the flux calibration, and the relative error of 20% on the combination of the uncertainties on the host-galaxy contribution and the unknown stellar population. We refer the reader to paper I for a detailed description of the intrinsic SED recovering and the optical/UV SED fitting analysis. We note that the disc spectrum at the spectral window of $0.2-0.8\,\mu$m is insensitive to the spin given the assumed uncertainties on the BH mass (0.5 dex) and the accretion rate (0.5 dex). Thus, the derived spin parameter are not very meaningful and shorter wavelengths are required to estimate the spin.

Our best fitted AD SED are shown in Fig. A1 and all the model parameters, including the disc luminosity, L_{AGN}, and the monochromatic luminosities at 2500 Å, are listed in Table A2. For J075101, J080101 and J081441, a quiescent galaxy model from the evolutionary spectral library of Charlot & Bruzual (1991) with an age of 11 Gyr provided sufficiently good fit to the stellar spectrum. On the basis of the "bluer" optical spectrum of J100055, the stellar population must be younger than 11 Gyr. A template with 1.4 Gyr and solar metallicity provides better fit to this spectrum and was adopted in this case. As we expected from our previous work (paper I), the simultaneous optical/UV SED of the SEAMBHs AGN, even those with the highest mass accretion rates, $\dot{\mathcal{M}} > 20$, can be fit by the simple optically thick, geometrically thin AD model. The declared good fits (see Fig. A1) still include small deviations of the model from the local continuum at some wavelengths. This is not surprising given the uncertainties on AD models, especially the radiative transfer in the disc atmosphere that was not treated here in detail, as well as on the choice of the host galaxy template.

A3 X-ray modelling

We performed an X-ray spectral analysis with XSPEC v12.8.2, using only the more accurately calibrated data at 0.3–10 keV. The source spectra for the three objects with the large number of counts were grouped to have at least 20 counts in each bin in order to apply the modified χ^2 minimization technique. For the lowest quality spectrum of J075101, with less than 400 counts, we used a minimum of 15 counts per bin instead of 20. All quoted errors are for a 90 per cent confidence interval for one parameter ($\Delta\chi^2 = 2.706$).

We first consider the hard X-ray (2–10 keV) band, and

[3] http://irsa,ipac.caltech.edu/applications/DUST

Table A2. Simultaneous optical/UV SED. Measured and deduced physical parameters while modelling the intrinsic reddening $E(B-V)$ with a classical SMC extinction curve and assuming an inclination of $\cos\theta$=0.75. For J080101 there is no contemporaneous optical spectrum, and only two OM photometric points thus no model could be derived.

Object	Host Galaxy		thin AD model							
	template	f [%]	$E(B-V)$ intrinsic	$\log M_{BH}$ [$M_\odot$]	$\log \dot{\mathcal{M}}$	η	χ^2_ν	$\log L_{AGN}$ [erg s^{-1}]	$\log L_{2500\text{Å}}$ [erg s^{-1}]	$\log L_{2\text{keV}}$ [erg s^{-1}]
J075101	11 Gyr	0.26	$0.120^{+0.240}_{-0.070}$	7.66	1.42	0.057	0.489	45.27	44.70	41.67
J081441	11 Gyr	0.32	$0.004^{+0.004}_{-0.004}$	7.28	1.38	0.321	2.803	45.41	44.54	43.67
J100055	1.4 Gyr	0.70	$0.000^{+0.010}_{-0.000}$	7.00	1.78	0.057	4.823	45.65	44.47	43.44

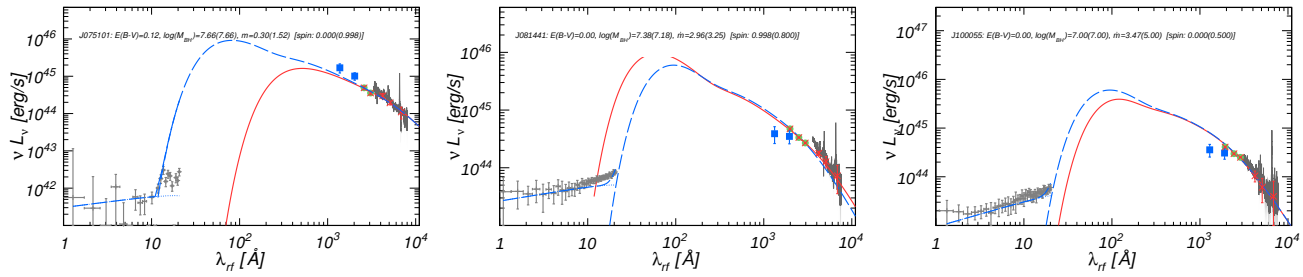

Figure A1. Simultaneous optical-to-X-ray SED with the best-fit thin AD model over-plotted assuming an inclination of $\cos\theta$ = 0.75. While the red line represents the best-fit thin AD models to the optical spectrum, the blue line represents the best fit to the optical-UV-X-ray SED assuming a power-law plus thin AD model as responsible of the hard-X-ray emission and the soft-X-ray-to-optical emission, respectively. Only the objects with simultaneous optical (green points: OM photometry; gray spectrum: Lijiang observations) and X-ray spectra are shown: J075101, J081441 and J100055, respectively. The blue square points represent the available non-contemporaneous UV photometry from GALEX which are not used in the fitting process.

apply a simple power law (PL) model (with neutral absorption fixed at the Galactic value, WABS) to all sources. In all the cases, we obtain a satisfactory descriptions of the hard X-ray emission which allows us to constrain the spectral photon index within an average error of 10%. We can not constrain the spectral slope of J075101 due to the poor signal-to-noise ratio above a few keV which results in a huge error on the slope and hence its optical-to-X-ray spectral slope, α_{OX}, can not be constrained. The extrapolation of the PL model to soft X-ray energies does not provides an adequate description of the entire (0.3–10 keV) X-ray data which highlights an excess emission to soft X-ray energies: the data below 2 keV lie in all cases above the extrapolated bet-fit hard PL. The hard X-ray spectra were also inspected for the presence of iron (Fe) emission lines. In all the objects an additional narrow emission line in the range 6.4–6.7 keV (neutral to highly ionized Fe) does not improve the significance of the fit. Because of this, we do not include an unresolved Fe Kα emission line in our spectral models.

In order to check the reliability of the soft excess, we refitted the whole 0.3–10 keV band with a simple PL model and compare it with a (phenomenological) broken power law (BPL). Then we also explore the possibility of X-ray absorption, however in no case the addition of a neutral absorption at the redshift of the source improved the quality of the fit, so intrinsic absorption covering entirely the X-ray source plays a negligible role in these RM-selected SEAMBHs. In Table A3 we report the spectral slopes in the soft, Γ_s, and hard, Γ_h, band for the broken PL model and the break energy which is in the 1.5–2 keV range. The spectral slopes of the best-fit PL model over the entire X-ray band were consistent with the soft slope of the BPL, Γ_s which dominate the fit due to the high signal-to-noise in the soft X-ray band. The BPL model is then a better description of the X-ray spectra of J080101, J081441 and J100055, while a single PL model is adequate for J075101 (at the 90.36 per cent level only). In other words, a soft excess is detected in J080101, J081441 and J100055, and not significantly present in J075101 due to the poor signal-to-noise in the hard X-ray band. The X-ray spectral slopes ($f_\nu \propto \nu^{\alpha_X}$) in the soft X-ray band, α_X=1.62–1.96, are consistent with the soft X-ray slope of NLS1, e.g. $\langle\alpha_X\rangle$ =1.58 with a 16th and 84th percentile of 1.11 and 2.16 found in the sample of Grupe et al. (2010) observed by *Swift XRT*. The hard spectral slope is also remarkably similar (α_X=1.10–1.27) to the typical spectral slopes of NLS1 (see e.g. Zhou & Zhang 2010, $\alpha_X \sim 1.04$). We conclude that the X-ray spectral shape of our RM-selected SEAMBHs differ significantly from the average properties of low accreting AGN but agree closely with the X-ray properties of NLS1s. We note that the broken PL is not entirely adequate to reproduce the soft excess and that results from such spectral fits should not be used to infer the significance of the soft excess detection. A black body (BB) or a compton thick cloud (CC) representation are a better, though also phenomenological, parametrization of the soft excess.

We attempted to fit the entire optical-UV-X-ray data of J075101, J081441 and J100055 using their contemporaneous optical/UV and X-ray observations that were presented here. The optical-UV part were modelled by the best-fit thin AD model with the spin as the only free parameter which was combined with a single power-law in order to fit simultaneously optical/UV and X-ray data sets. Our simultane-

Table A3. Model parameters of the soft X-ray excess. Galactic absorption is always assumed (WABS). Unabsorbed luminosities are given in units of 10^{43} erg s^{-1} in the soft (0.5–2 keV) and hard (2–10 keV) energy bands. Following the work of Vasudevan et al. (2013), the term L_{BB}/L_{PL} is defined as the ratio of the luminosity of the feature (using a black-body to model it) from 0.4–3 keV, to the luminosity in a relatively "clean", featureless portion of the primary power law from 1.5–6 keV.

Model†	Object	Energy Band [keV]	free paramaters Γ_s	E_{break} [keV]	Γ_h	kT_e [keV]	χ^2_ν	$L_{BB}/L^{\dagger}_{PL}$	$L_{0.5-2\ \mathrm{keV}}$ [10^{43} erg s^{-1}]	$L_{2-10\ \mathrm{keV}}$ [10^{43} erg s^{-1}]
PL	J075101	1.5–10	-	-	$2.20^{+5.56}_{-2.08}$	-	1.541		0.04	
		0.5–10	$3.42^{+0.21}_{-0.18}$	-	-	-	1.233			
	J080101	2.0–10	-	-	$2.09^{+0.12}_{-0.07}$	-	1.296		3.60	
		0.5–10	$2.90^{+0.02}_{-0.02}$	-	-	-	1.993			
	J081441	2.0–10	-	-	$2.08^{+0.07}_{-0.07}$		1.160		5.31	
		0.5–10	$2.56^{+0.03}_{-0.01}$	-	-	-	1.537			
	J100055	2.0–10	-	-	$2.27^{+0.17}_{-0.16}$	-	0.780		2.82	
		0.5–10	$2.63^{+0.03}_{-0.05}$	-	-	-	1.040			
BPL	J075101	0.5–10	$2.62^{+0.60}_{-0.54}$	$0.79^{+0.13}_{-0.11}$	2.2	-	1.184		3.68	0.04
	J080101	0.5–10	$2.96^{+0.02}_{-0.02}$	$1.66^{+0.10}_{-0.13}$	$2.23^{+0.30}_{-0.15}$	-	1.413		10.96	3.61
	J081441	0.5–10	$2.62^{+0.02}_{-0.02}$	$2.34^{+0.58}_{-0.70}$	$1.97^{+0.18}_{-0.18}$	-	1.323		9.29	5.33
	J100055	0.5–10	$2.68^{+0.04}_{-0.04}$	$2.40^{+0.79}_{-0.70}$	$2.31^{+0.23}_{-0.29}$	-	0.975		2.04	0.97
BB	J075101	0.5–10	-	-	2.2	$0.132^{+0.013}_{-0.014}$	1.170	< 4.49	0.18	0.04
	J080101	0.5–10	-	-	$2.27^{+0.04}_{-0.04}$	$0.124^{+0.002}_{-0.002}$	1.292	1.39	7.94	3.55
	J081441	0.5–10	-	-	$2.25^{+0.04}_{-0.04}$	$0.132^{+0.004}_{-0.004}$	1.307	0.59	8.64	5.20
	J100055	0.5–10	-	-	$2.52^{+0.07}_{-0.08}$	$0.114^{+0.009}_{-0.010}$	0.992	0.47	2.03	0.91

† XSPEC definition: PL) WABS*ZWABS*POWERLAW; BPL) WABS*ZWABS*BKNPOWER; BB): WABS*(ZBBODY+POWERLAW)

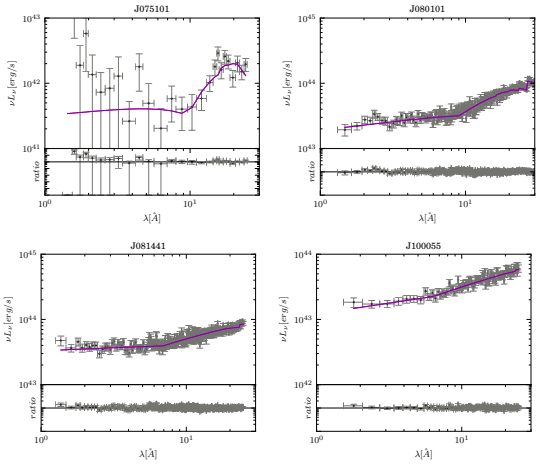

Figure A2. *XMM-Newton* spectra, best fitted broken-power law models and residuals for J075101, J080101, J081441 and J100055. The upper panels of each row show the results of the X-ray spectral fitting to the EPIC-pn spectra. The lower panels of each row show the data/model ratio of each data set.

ous best fits are shown in Fig. A1. Although the addition of the disc component to the X-ray emission improved the fit, our best-fit continuum model significantly under-predicts the soft emission. This suggests that the AD can not explain the total emission of the soft X-ray. In fact, SEAMBHs AD are predicted to be "slim" and their extreme UV spectra are not fully understood. Because of the limited band of the X-ray data, and the large uncertainties on slim disc SEDs, we are not in a position to resolve this issue by accurate spectral fitting of the data. In fact, the SEAMBHs systems modelled by paper I, do not show any (indirect) indications that their far UV luminosity is unusually high compared with the far-UV luminosity of sub-Eddington systems. This might mean that this "soft excess" is not part of the big blue bump, however we think that the most likely explanation is that SEAMBHs do not host thin disc, being in good agreement with the broad underlying assumption that SEAMBHs are the best candidates to host slim disc geometries.

An additional consistency check can be obtained by studying the soft X-ray emission as a thermal emission of a Compton thin plasma with certain temperature kT_e. In this case, we consider a simple continuum model comprising a power-law plus black-body (ZBBODY) emission to model the prominent soft excess. The addition of this thermal component to the PL model improved the fit, providing an excellent fit in all the cases (see table A3 model BB). We find that the best-fit X-ray spectral index is also steep ($\alpha_X = 1.2 - 1.5$) and consistent within error to that obtained by fitting a simple power-law model to the hard X-ray band data. The best-fit to this model for the source with no need for a soft excess (J075101) was also computed. Finally, we parametrize the strength of the soft excess, L_{BB}/L_{PL}, following Vasudevan et al. (2013) by the ratio of the luminosity of the feature (using a black-body to model it) from 0.4–3 keV, to the luminosity in a relatively "clean", featureless portion of the primary power law from 1.5–6 keV. We find that the strength of the soft excess range from a factor 0.47 up to 1.4, and despite the small size of the SEAMBHs, the average of the BB contribution in the 0.5–2 keV clusters around a factor 0.8 being higher than previous studies (Vasudevan et al. 2013). In the case of J075101 (where there is no need for soft excess) the BB contribution is only an upper limit of a factor 4.5. We find that the inferred temperature of the soft excess clusters with very little dispersion around 114–143 eV with an average of 128 eV, while the disc luminosity of our sample

spans about two orders of magnitude. Although 128 eV is a reasonable value for the disc temperatures around our objects, it is quite remarkable that the inferred temperature is very similar to that of PG quasars, casting doubts on its interpretation in terms of thermal emission (Vasudevan et al. 2013).

This paper has been typeset from a TEX/LATEX file prepared by the author.